ACS Catalysis

Research Article

pubs.acs.org/acscatalysis

Coordination Geometry and Oxidation State Requirements of Corner-Sharing MnO_6 Octahedra for Water Oxidation Catalysis: An Investigation of Manganite (γ-MnOOH)

Paul F. Smith,[†] Benjamin J. Deibert,[†] Shivam Kaushik,[†] Graeme Gardner,[†] Shinjae Hwang,[†] Hao Wang,[†] Jafar F. Al-Sharab,[‡] Eric Garfunkel,[†,§] Laura Fabris,[§] Jing Li,[†] and G. Charles Dismukes*[,†,∥]

[†]Department of Chemistry and Chemical Biology, Rutgers, the State University of New Jersey, 610 Taylor Road, Piscataway, New Jersey 08854, United States

[‡]Department of Engineering Technology, Northwestern State University, 205 Williamson Hall, Natchitoches, Louisiana 71497, United States

[§]Department of Materials Science and Engineering, Rutgers, the State University of New Jersey, 607 Taylor Road, Piscataway, New Jersey 08854, United States

[∥]The Waksman Institute, Rutgers, the State University of New Jersey, 190 Freilinghuysen Road, Piscataway, New Jersey 08854, United States

Supporting Information

ABSTRACT: Surface-directed corner-sharing MnO_6 octahedra within numerous manganese oxide compounds containing Mn^{3+} or Mn^{4+} oxidation states show strikingly different catalytic activities for water oxidation, paradoxically poorest for Mn^{4+} oxides, regardless of oxidation assay (photochemical and electrochemical). This is demonstrated herein by comparing crystalline oxides consisting of Mn^{3+} (manganite, γ-MnOOH; bixbyite, Mn_2O_3), Mn^{4+} (pyrolusite, β-MnO_2) and multiple monophasic mixed-valence manganese oxides. Like all Mn^{4+} oxides, pure β-MnO_2 has no detectable catalytic activity, while γ-MnOOH (tetragonally distorted $Mn^{3+}O_6$, D_{4h} symmetry) is significantly more active and Mn_2O_3 (trigonal antiprismatic $Mn^{3+}O_6$, D_{3d} symmetry) is the most active. γ-MnOOH deactivates during catalytic turnover simultaneous with the disappearance of crystallographically defined corner-sharing $Mn^{3+}O_6$ and the appearance of Mn^{4+}. In a comparison of 2D-layered crystalline birnessites (δ-MnO_2), the monovalent Mn^{4+} form is catalytically inert, while the hexagonal polymorph, containing few out-of-layer corner-sharing $Mn^{3+}O_6$, has ~10-fold higher catalytic activity than the triclinic polymorph, containing in-plane edge-sharing $Mn^{3+}O_6$. These electronic and structural correlations point toward the more flexible (corner-shared) $Mn^{3+}O_6$ sites, over more rigid (edge-shared) sites as substantially more active catalytic centers. Electrochemical measurements show and ligand field theory predicts that, among corner-shared $Mn^{3+}O_6$ sites, those possessing D_{3d} ligand field symmetry have stronger covalent Mn−O bonding to the six equivalent oxygen ligands, which we ascribe as responsible for more efficient and faster electrolytic water oxidation. In contrast, D_{4h} $Mn^{3+}O_6$ sites have weaker Mn−O bonding to the two axial oxygen ligands, have separated electrochemical oxidation waves for Mn and O, and are catalytically less efficient and exhibit slower catalytic turnover. By controlling the ligand field geometry and strength to oxygen ligands, we have identified the key variables for tuning water oxidation activity by manganese oxides. We apply these findings to propose a mechanism for water oxidation by the $CaMn_4O_5$ catalytic site of natural photosynthesis.

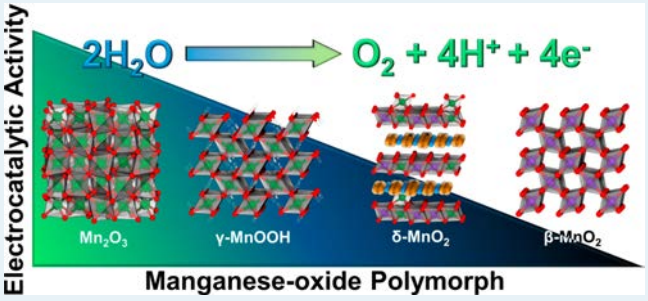

KEYWORDS: *manganese oxide, water oxidation, Jahn−Teller distortion, birnessite equilibria, electrocatalysis, photosystem II*

INTRODUCTION

The omnipresent $CaMn_4O_5$ water oxidation catalyst in natural photosystems has inspired the development of Mn oxides as artificial catalysts. Multiple reports now show there exists a correlation between Mn^{3+} content and catalytic activity for the oxygen evolution reaction (OER).[1−14] Strategies to improve activity from Mn oxides thus must consider stabilizing Mn^{3+} against the disproportionation reaction into inactive Mn^{4+} and Mn^{2+} species (eq 1).

$$2Mn^{3+}OOH + 2H^+ \leftrightarrow Mn^{4+}O_2 + Mn^{2+} + 2H_2O \quad (1)$$

Independent of catalysis applications, this reversible equilibrium has been studied by a number of groups, and commonly, Mn^{3+}OOH intermediates have been identified[15] or isolated as products.[16−20] The isolated compounds allow testing whether

Received: January 11, 2016
Published: February 16, 2016

DOI: 10.1021/acscatal.6b00099
ACS Catal. 2016, 6, 2089−2099

Mn^{3+} in a crystallographically defined structure is more active than in others. We sought to pursue this line of research, as we have shown the spinel $LiMn_2O_4$ (~50% Mn^{3+}) is an exception to the general trend: it is a very poor water oxidation catalyst in both photochemical[21] and electrochemical[6] assays.

The most stable polymorph of MnOOH is manganite (γ-MnOOH), space group $P2_1/c$. The γ-MnOOH structure consists of corner-linked $Mn^{3+}O_6$ octahedral chains that form proton-containing 1 × 1 rhombohedral tunnels (Figure 1). γ-MnOOH can be considered as a reduced ($1e^- + 1H^+$), quasi-isostructural derivative of pyrolusite (β-MnO_2, space group $P4_2/mnm$) in which the 1 × 1 tunnels are nearly rectangular. γ-MnOOH has elongated octahedra as a result of the $3d^4$ valence electronic asymmetry (Jahn−Teller distortion) and hydrogen bonding.[22] Each octahedron in γ-MnOOH possesses two long (2.27 Å) and four short (1.93 Å) Mn−O bonds (2.04 Å average), yielding an 8% increase over the symmetrical Mn^{4+} sites in β-MnO_2 (1.89 Å average). The Mn−Mn distance is also elongated, though more so for corner-sharing octahedra (9%, 3.76 vs 3.42 Å) than for edge-sharing octahedra in the same chain (2.88 vs 2.87 Å).

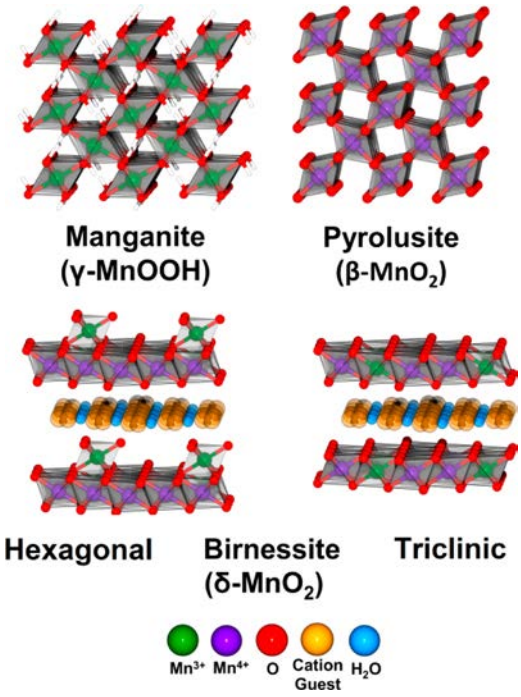

Figure 1. Structural depictions of several Mn oxides.

The presence of corner-sharing Mn octahedra in amorphous electrodeposited manganese oxides (sometimes referred to loosely as birnessite-like) has been correlated with water oxidation activity in the EXAFS studies by Dau and co-workers.[23] Crystallographically defined birnessites having long-range order provide a complementary approach for studying corner-shared Mn^{3+} octahedra, as there exist two structural archetypes: hexagonal (HexBir) and triclinic (TriBir). Both materials consist of sheets of edge-sharing MnO_6 octahedra separated by interstitial hydrated cations (Figure 1). TriBir contains edge-shared Mn^{3+} octahedra within the MnO_2 sheets, while the reduced charge is compensated by interlayer spectator cations (here, K^+). In contrast, HexBir contains higher Mn^{4+} content and as a result does not stabilize distorted Mn^{3+} within sheets; instead, these Mn^{3+} are located above or below cationic sheet vacancies in the interlayer (or surface) bonded via corner-sharing bridges. Hexagonal birnessites are, in general, poorly crystalline due to the potential buildup of disordered vacancies. Poorly crystalline birnessites correlate with higher catalytic activity in multiple studies,[24−28] in contrast to triclinic birnessites which are reported to exhibit low (or zero) activity for water oxidation.[4,24,29] Collectively, these results predict corner-sharing Mn^{3+} are highly active catalytic sites.

We report here the results of three investigations of corner-shared Mn^{3+} polytypes in crystalline ordered environments, demonstrating quantitative correlation with water oxidation activity above pH 7. In the first two series of experiments, γ-MnOOH shows a significantly lower overpotential than β-MnO_2 for both electrocatalytic and photocatalytic water oxidation. In the third investigation, a crystalline hexagonal structural archetype of birnessite shows a significantly higher rate of photolytic water oxidation than the triclinic form. Collectively, these results clearly demonstrate that corner-sharing Mn^{3+} octahedra are the main predictor for water oxidation catalysis, while buried edge-sharing Mn^{3+} and corner-sharing Mn^{4+} are not significant contributors. Few reports are available that test $Mn^{3+}O_6$ polytypes in structurally well-defined (crystalline) materials,[4,29] and only one report has examined pure phase manganite for water oxidation (though structural characterization was absent in that case).[30]

RESULTS

Synthesis and Characterization. Of several techniques examined, we found the synthetic method described by Suib et al.[31] produces a brown powder which gives a PXRD pattern (Figure 2A) that agrees, in both peak positions and intensities, with a MnOOH structural reference (ICSD-84949).[22] Consistent with the report of Suib et al., SEM images indicated a nanostructured material with pill-shape morphology of average dimensions 150 nm x 30 nm (Figure 2B and Figure S1 in the Supporting Information). High-resolution transmission electron microscopy (HRTEM) and SAED patterns further confirmed γ-MnOOH lattice spacings (Table S1 in the Supporting Information) and showed atomic structural homogeneity (Figure 2C and Figure S1). TEM indicates crystallites 15−20 nm in size, in agreement with values calculated from the PXRD line width using the Scherrer equation. The Raman spectrum of γ-MnOOH (vide infra) exhibits peaks at 357, 388, 530, 558, and 621 cm^{-1}, in excellent agreement with the literature.[32,33] The sample has a surface area of 50 m^2/g, as determined by BET N_2 gas absorption (Figure S2 in the Supporting Information).

Electrocatalysis. The OER activity of this phase was tested via electrochemical techniques (pH 7 and 14) and by using a well-known assay based on photooxidation of $Ru(bpy)_3^{2+}$ (bpy = 2,2′-bipyridine) in buffered persulfate (pH 7).[34] γ-MnOOH is known to disproportionate to MnO_2 below pH 6;[35−38] hence, no assays below this pH were pursued. Figure 3 shows that thin films of γ-MnOOH nanoparticles (supported within pH-neutralized Nafion) on glassy-carbon electrodes exhibit significant catalytic activity for water oxidation at pH 7 and 14. We adopt as a benchmark the overpotential required for 10 mA/cm^2 current density,[39,40] which γ-MnOOH electrodes with 0.5 mg/cm^2 loading achieved at η = 530 mV (1 M NaOH) and 680 mV (1 M phosphate buffer). The observed oxidation curve (Figure 3) produces O_2 as measured by gas chromatography (Figure S3 in the Supporting Information). At 550 mV overpotential, a Faradaic efficiency of 97% was obtained, as

DOI: 10.1021/acscatal.6b00099
ACS Catal. 2016, 6, 2089−2099

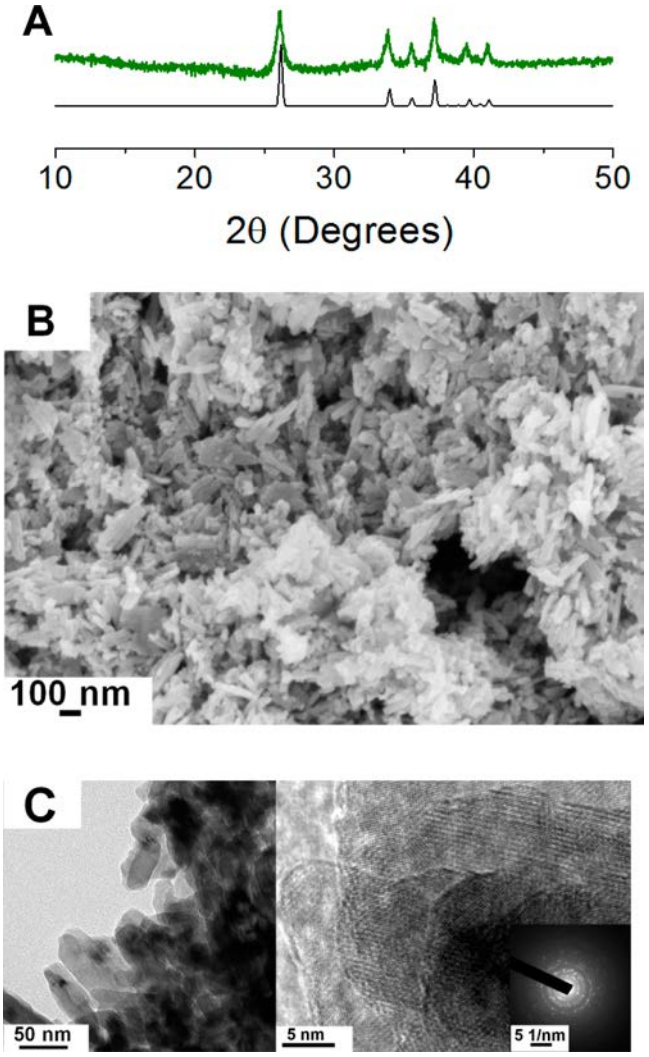

Figure 2. γ-MnOOH structural characterization: (a) PXRD of as-made sample (green) and structural reference[22] (black), with space group $P2_1/c$; (b) SEM (bottom left) and (c) HRTEM showing morphology (left) and crystallinity (right) with SAED (bottom inset).

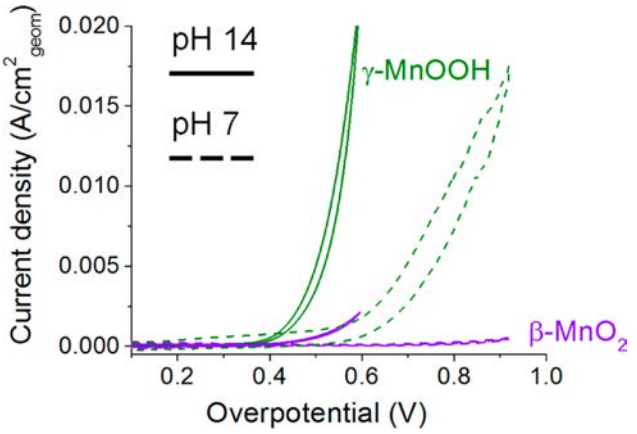

Figure 3. Cyclic voltammograms (10 mV/s, *iR* corrected) for the 1 × 1 tunnel manganese oxides of Figure 1 in 1 M NaOH or 1 M phosphate buffer, with loading 0.5 mg/cm^2. Conditions: 5 mm glassy-carbon working electrode, Ti counter electrode, reference electrodes Hg/HgO (pH 14, E_{ref} = +0.100 V vs NHE) and Ag/AgCl (pH 7). The silver reference electrode was externally calibrated vs SCE (E_{ref} = +0.240 V vs NHE). Overpotentials are corrected for the pH dependence of water oxidation and given relative to each reference electrode using the expression (measured potential) − (1.23 V − (0.059 × pH) − E_{ref}). The current is normalized to the geometric electrode area.

calibrated against O_2 produced from identical charge passed by an Ir/C anode (80 m^2/g, Premetek).

The application of an oxidizing potential to γ-MnOOH could be hypothesized to form β-MnO_2. The literature is divided over the efficacy of β-MnO_2 to catalyze water oxidation,[4,26,41−43] though this discrepancy can partially be ascribed to different testing conditions, as recently concluded by Stahl et al.[29] Phase-pure β-MnO_2 that we isolated previously was inactive in water oxidation and only demonstrated activity in the presence of an Mn_2O_3 impurity.[4] In the present study, we show that several variables quantitatively correlate the water oxidation activity to Mn^{3+} content in γ-MnOOH. First, Figure 3 shows that, under electrochemical oxidation conditions, monophasic β-MnO_2 did not exhibit any activity above baseline in comparison to monophasic γ-MnOOH at identical mass loading. Second, cyclic voltammograms of γ-MnOOH consist solely of the water oxidation curve with no resolved $Mn^{3+} \rightarrow Mn^{4+}$ prefeature at potentials between open circuit and the onset of catalytic current. Integration of the total charge passed in this region at pH 14 indicates a maximum of 1% Mn^{4+} could form or 17% Mn^{4+} if only surface Mn^{3+} was oxidized (see the Supporting Information for calculations). We note that this is an upper bound because non-Faradaic current is the sum of several charge accumulation processes on the electrode surfaces, including adsorption, double-layer formation, and possibly pseudocapacitance. Third, we fabricated electrodes using γ-MnOOH that had been presonicated in the presence of 2.5 equiv of $Na_4P_2O_7$, a strong chelator of Mn^{3+} that prevents its oxidation. This gave only background levels of current (Figure S4 in the Supporting Information).

If voltammograms are scanned reductively (below open circuit) under an N_2 atmosphere, β-MnO_2 exhibits a $Mn^{4+} \rightarrow Mn^{3+}$ transition at 0.6 V vs RHE (Figure S5 in the Supporting Information). Subsequent oxidative scanning results in the $Mn^{3+} \rightarrow Mn^{4+}$ transition, as clearly visible at 1.2 V vs RHE (0 V overpotential). This analysis suggests that water oxidation by γ-MnOOH occurs because its $Mn^{3+} \rightarrow Mn^{4+}$ potential is shifted to higher potential energy (≥400 mV) owing to stronger mixing (hybridization) of the Mn and O orbitals than in β-MnO_2. As a result of this stronger admixing within this Mn−O antibonding band, oxidation leads to O-centered reactions, leading to O−O bond formation and ultimately O_2 release. In contrast, the $Mn^{3+} \rightarrow Mn^{4+}$ transition at lower potential energy suggests less strong admixing with O orbitals, leading to a larger barrier to O−O bond formation.

The current density and O_2 rate from the γ-MnOOH film electrode gradually deactivates during repetitive CV cycling through the water oxidation curve or during bulk electrolysis at O_2-evolving potentials (Figure S6 in the Supporting Information). At pH 14 and 500 mV applied overpotential, films showed a gradual, continuous decrease in activity from 5 to 1.9 ± 0.4 mA/cm^2 over 20 min, corresponding to a total charge passed of 2−3 e$^-$/Mn. This gradual loss of 60% activity is attributed to inactivation of the γ-MnOOH, as no evidence for film delamination or minimal Mn leeching was detected. Namely, (1) films prepared identically except containing more robust catalysts sustained constant initial current densities beyond 20 min,[6] (2) delamination of robust catalyst films at

DOI: 10.1021/acscatal.6b00099
ACS Catal. 2016, 6, 2089−2099

high O_2 bubbling rates invariably occurs as sharp, sudden loss of current (Figure S6), in contrast to this gradual deactivation, (3) sonication of electrode films in water failed to remove samples from the electrode and did not affect initial currents (vs sonication in ethanol, which allowed isolation of post-reaction samples, see below), and (4) ICP-OES analysis of the postreaction electrolyte revealed only minor quantities of the total Mn originally loaded onto the electrode (between 0.02−0.1%), far less than the 60% catalytic deactivation. We thus correlate this electrochemically induced loss in catalytic activity to structural and oxidation state changes of γ-MnOOH, as described next.

Postreaction Characterization. We characterized γ-MnOOH-containing films after passing 0, 2, and 4 charge equivalents/Mn at 550 mV overpotential in 1 M NaOH. PXRD positively identified γ-MnOOH in the unreacted films, which correlate with the highest electrochemical activity. As more charge is passed, and electrochemical activity decreases, the γ-MnOOH PXRD peaks decrease in intensity (Figure S7 in the Supporting Information). In the most deactivated sample (15% initial activity and passed $4e^-$/Mn), there is no visible crystalline phase of any Mn oxide identified by PXRD.

For greater surface sensitivity, HRTEM was utilized. The reacted surface contained significant disorder, as evidenced by decreased intensity of well-defined spots in the FFT pattern (Figure 4). This disorder was heterogeneous across the sample,

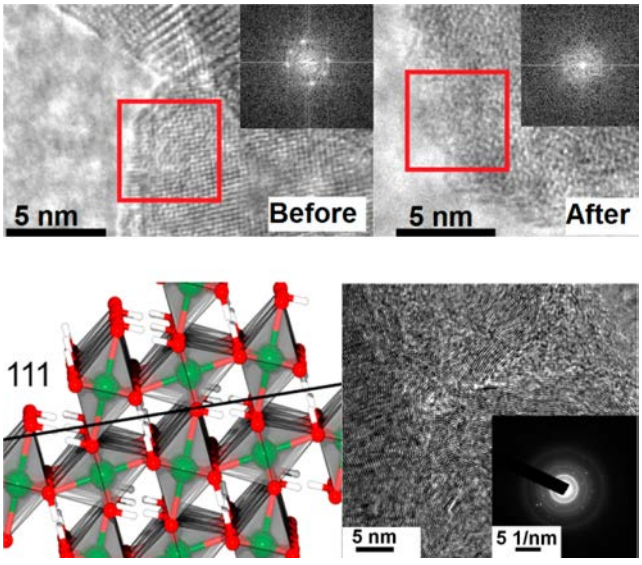

Figure 4. HRTEM characterization: (top) the γ-MnOOH surface before and after electrocatalysis, $4e^-$/Mn passed; (bottom left) the 111 cut plane showing the protons, with oxygen in red and manganese in purple; (bottom right) Ppostreaction sample HRTEM and SAED pattern.

ranging from 2 nm surface coverage to extended networks where lattice fringes showed significant curvature (Figure 4, bottom right). Overall, micrographs of the bulk revealed a high degree of uniformly spaced 2-D layers within individual domains and with random orientations (semicrystalline) and sizes (Figure 4 and Figure S8 in the Supporting Information).

Domains of crystallinity, where detected, were smaller in size (<33%) relative to the starting material. These domains showed increases in *d* spacings, though small (~2%). The most prominent SAED spacing we observed refers to the plane containing the protons within the tunnels (Figure 4, bottom left). This suggests that protons can be removed from tunnels during catalysis, leaving behind an expanded structure with reduced hydrogen bonding.

Vibrational Spectroscopy. Further evidence describing the nature of the structural transformation upon electrolysis was obtained by vibrational spectroscopy. Resonance Raman (RR) spectroscopy was conducted using 514 nm light, which is resonant with the O → Mn charge transfer electronic absorption band of γ-MnOOH (Figure 5). The vibrational spectrum is quite simple, exhibiting only five resolved peaks between 0 and 1000 cm^{-1}, in excellent agreement with the literature.[32,33]

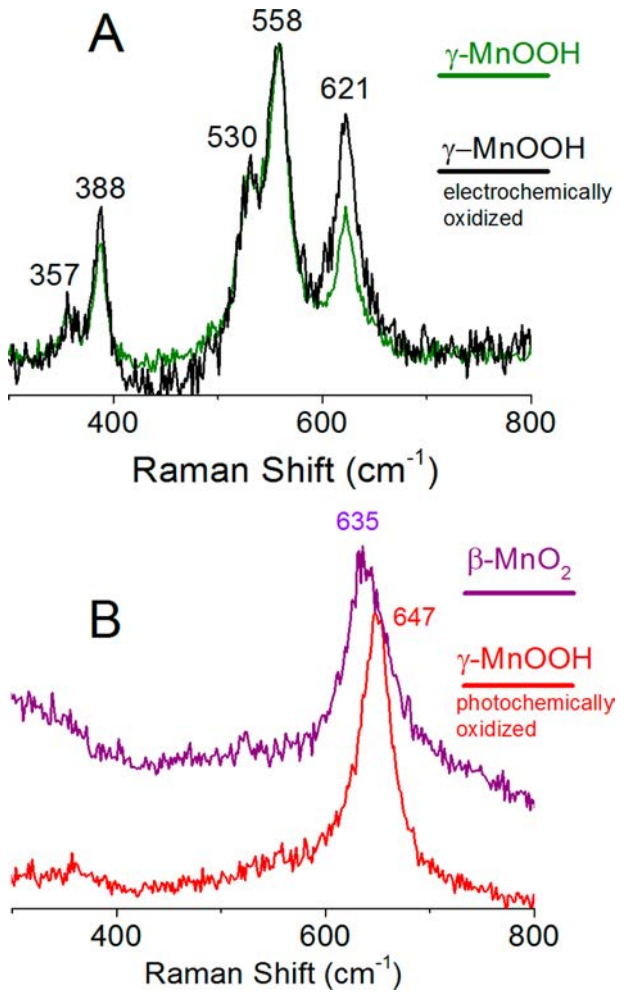

Figure 5. (A) Representative resonance Raman spectra of γ-MnOOH before (green) and after (black) O_2 evolution electrocatalysis, $2e^-$ passed per Mn. The after sample required 5× longer accumulation time for the signal to appear; resulting spectral intensities are normalized at 558 cm^{-1}. Five peaks were resolved within 200−1000 cm^{-1} with no apparent peaks elsewhere. (B) Resonance Raman spectra of γ-MnOOH after O_2 evolution by reaction with photocatalysis assay medium (red) and unreacted β-MnO_2 (purple).

As the electrolysis reaction at the γ-MnOOH electrode proceeds, there is a nonuniform loss of intensity of all vibrational peaks, on the same time scale for which both the PXRD and TEM data indicate loss of identifiable γ-MnOOH domains. Normalization of the spectra at the 558 cm^{-1} peak reveals a relative increase (less loss) in the intensity of the 621

DOI: 10.1021/acscatal.6b00099
ACS Catal. 2016, 6, 2089−2099

cm^{-1} peak and to a much lesser extent the 388 cm^{-1} peak. To our knowledge, assignments of the vibrational modes for γ-MnOOH have not been made previously. On the basis of comparisons to reference compounds[44,45] and other crystalline manganese oxides,[46−48] the two bands below 450 cm^{-1} correspond to terminal Mn−O(H) tunnel and surface stretches, while the three bands between 500 and 1000 cm^{-1} correspond to Mn−O−Mn core modes. On the basis of their frequencies, the two bands in manganite at 558 and 530 cm^{-1} can be tentatively assigned as the symmetric stretching modes of the "long" $[MnOMn]^{4+}$ bridges from two types of longer 2.27 Å Mn−O bonds (Figure 1). The 558 cm^{-1} frequency exactly matches this mode in $[Mn^{III}_2(Hpbz)_2(\mu\text{-}O)(\mu_{1,2}\text{-}OAc)_2]^{2+}$ (assigned on the basis of μ-^{18}O substitution and normal coordination analysis).[45,49]

The strong 621 cm^{-1} band may represent the corresponding asymmetric stretch which typically appears in the range 80−150 cm^{-1} to higher frequency, depending upon the number of μ-O bridges, their Mn−O−Mn angle, and Mn oxidation state. However, an alternative assignment is the symmetric stretch of the "short" $[MnOMn]^{4+}$ bridges through the 1.93 Å short Mn−O bonds (Figure 1).[50] This latter assignment is more likely, given the greater number of short Mn−O−Mn bridges per octahedron (4 vs 2 long) and the RR selection rule favoring enhancement of symmetric over asymmetric modes. For reference, the RR spectrum of pristine β-MnO_2 is shown in Figure 5B. Only a single broad band[51−53] is resolved at ∼635 cm^{-1}, in addition to weak unresolved absorption below 400 cm^{-1}. This simplification to a single Mn−O−Mn symmetric stretching mode is consistent with the higher symmetry lattice (Figure 1) with uniform distribution of "short" Mn−O bond distances (all 1.89 Å).

Adopting this latter assignment provides a self-consistent explanation for why the 621 cm^{-1} band grows as catalytic turnover proceeds: long Mn−O bonds are replaced by short Mn−O bonds. For the same reason, the smaller relative increase in the higher frequency terminal Mn−O(H) mode at 388 cm^{-1} as catalysis proceeds is consistent with the higher population of shorter terminal Mn−O(H) bonds. Collectively this characterizes the postreaction material as partially deprotonated and with higher overall average oxidation state.

XPS. For γ-MnOOH, the experimentally obtained XPS Mn $2p_{3/2}$ peak binding energy of 641.8 eV (Figure 6A) agrees with literature values obtained for Mn^{3+} in oxide (Mn_2O_3, 641.7−641.9 eV)[54] and as Mn^{3+} acetate (Sigma-Aldrich). Further, this peak was retained after loading into Nafion (Figure S9 in the Supporting Information). Following electrocatalysis, the binding energy shifts to a higher value (642.2 eV, Figure 6B), indicating a higher average oxidation state. This lies within the range (641.9−642.6 eV) commonly ascribed to Mn^{4+}.[54] Consistent with this assignment, pure-phase β-MnO_2 exhibits a prominent shoulder peak at 642.7 eV (Figure 6C). We thus assign the appearance of Mn^{4+} in the postreaction sample.

For a more quantifiable surface average oxidation state (AOS), we deconvoluted the Mn $2p_{3/2}$ peak into Mn^{2+}, Mn^{3+}, and Mn^{4+} components, using the curve-fitting procedure by Nesbitt and Banerjee.[55] This gives AOS values of 2.9 and 3.0 for γ-MnOOH with and without Nafion, respectively, vs 3.2 for electrochemically cycled γ-MnOOH, further indicative of oxidation to Mn^{4+} (see Table S2 in the Supporting Information). We could not gain information from the O_{1s} signal due to interference from the Nafion SO_4 groups.

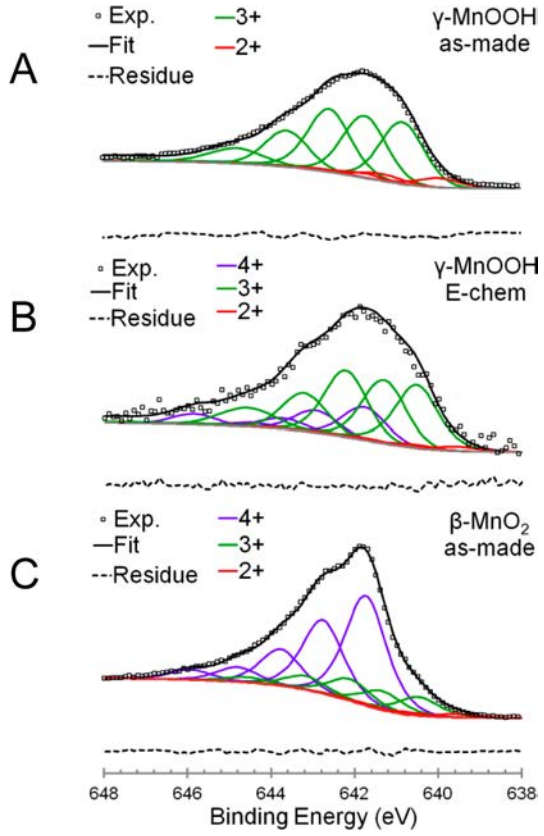

Figure 6. Mn $2p_{3/2}$ region of XPS spectra comparing γ-MnOOH (A), β-MnO_2 (C), and electrochemically oxidized γ-MnOOH (B). These spectra are deconvoluted into contributions from Mn^{4+} (purple), Mn^{3+} (green), and Mn^{2+} (red) via the method of Nesbitt and Banerjee[55] as described previously.[28]

Photocatalysis. In order to eliminate possible unknown complications from the electrode configuration, we expanded our study of water oxidation to photocatalysis, using γ-MnOOH particles suspended in homogeneous aqueous solutions of bicarbonate buffer (0.1 M pH 7). We used an established photochemical assay[4] to generate $[Ru(bpy)_3]^{3+}$ from $[Ru(bpy)_3]^{2+}$ (0.5 mM) and the electron acceptor $Na_2S_2O_8$ (10 mM). Clark electrode experiments confirm that γ-MnOOH catalyzes O_2 evolution under these conditions (Figure 7, left).

The photochemical assay provides a different approach to characterize the transformation of γ-MnOOH following O_2

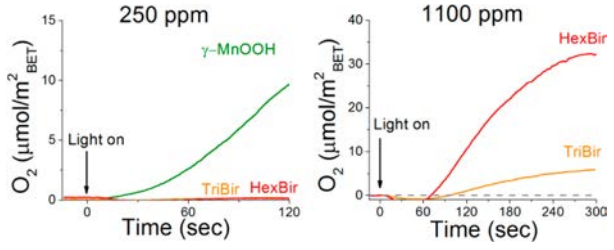

Figure 7. Photoinduced O_2 production from chemical oxidation of Mn oxides: (left) comparison of activities for both birnessites vs γ-MnOOH at the loading reported in ref 4; (right) higher total Mn loading results in O_2 evolution above background for both birnessites (the dashed gray line indicates the extrapolated baseline). Conditions: 0.5 mM $Ru(bpy)_3^{2+}$, 10 mM $Na_2S_2O_8$, 0.1 M pH 7 bicarbonate buffer.

DOI: 10.1021/acscatal.6b00099
ACS Catal. 2016, 6, 2089−2099

evolution catalysis, as it depends upon physical collisions of the oxidant and catalyst. Light is used to generate the oxidant in situ but is also absorbed by γ-MnOOH and may contribute to the reactivity. Because the γ-MnOOH tunnel size is too small to accommodate $Ru(bpy)_3$ (11 Å diameter), only the surface can be expected to oxidize initially and subsequent electron transfer from the bulk to surface could lead to deeper oxidation, possibly enhanced by the +3 surface charge from the Ru^{3+} oxidant molecule. Hence, this may not produce a result identical with that from the electrochemical system.

After 30 min of illumination and 5 $O_2/Mn_{surface}$ (1/4 O_2/Mn_{total}) produced, the postcatalysis PXRD pattern indicates extensive loss of crystallinity, seen as peak broadening, yet without formation of a new crystal phase (Figure S10 in the Supporting Information). XPS of the photochemically oxidized γ-MnOOH (Figure S11 in the Supporting Information) indicated an AOS increase from 3 to 3.4, and the Mn $2p_{3/2}$ binding energy shifts positively from 641.8 to 642.0. As this sample lacks a Nafion component, we were also able to measure the binding energy separation (ΔE) for manganese $2p_{3/2}$ and oxygen 1s. ΔE increases from 110.5 to 112.8 eV, further verifying a higher AOS for the postreaction sample. Mn oxides of higher AOS show ΔE values larger than those for more reduced species, due both to a shift of Mn to higher binding energies and a shift of O to lower binding energies.[56]

The five Raman peaks of γ-MnOOH disappear in photochemically treated samples and are replaced with a strong peak resembling that of the pristine β-MnO_2 sample (Figure 5B). Attempts to detect the unmodified Raman modes from bulk γ-MnOOH by focusing the beam more deeply into the sample were unsuccessful. Instead, the lone detected peak shifted within the range 636−657 cm^{-1}. Further, the lack of a prominent band from 540 to 600 cm^{-1} indicates loss of the Mn−O−Mn symmetric stretching mode characteristic of the long bonds to Mn^{3+}. Collectively, these results indicate that the photochemically induced transformation extends from the surface into the bulk and can be described as formation of a higher symmetry but more a disordered phase enriched in Mn^{4+} ("β-MnO_2 like").

These Raman results are complementary to both XPS measurements showing higher Mn^{4+} content, as well as with XRD, which does not detect a well-formed crystalline β-MnO_2 sideproduct. Thus, our TEM, Raman, and XRD data give consistent evidence for a structural change induced by oxidation. This change extends deeper into the bulk when achieved by illumination plus surface chemical oxidation, suggesting that light may contribute to overcoming a kinetic barrier for the structural transition initiated by Ru^{3+} oxidizing Mn^{3+}.

Catalyst Benchmarking. The BET-surface-normalized photochemical turnover frequency (TOF)/m^2 of γ-MnOOH as measured by the method described in our previous report[4] is comparable to phase-pure spinel Mn_3O_4 (hausmannite). We also observed comparable electrochemical activity for Mn_3O_4 and γ-MnOOH at pH 7 (Figure 8 and Figure S12 in the Supporting Information). In alkali, the two compounds also performed comparably at overpotentials <500 mV (Figure S12). The electrochemistry of Mn_3O_4 is otherwise known from Ramirez and Fiechter et al.,[57] and our result of 5 mA/cm^2 at η = 550 mV compares favorably to that report.

These results were further extended across six manganese oxide compounds at pH 7, which revealed a correlation between photochemically driven and electrochemically driven water oxidation rates (Figure 8). This trend was also found to hold at pH 14 (Figure S13 in the Supporting Information). Atop both trend lines is bixbyite Mn_2O_3, which has a BET surface area equal to or less than those of Mn_3O_4 and γ-MnOOH. This material attained 10 mA/cm^2 at η = 450 mV in alkali (Figure S14 in the Supporting Information), a value which compares favorably to those in recent literature.[3,57]

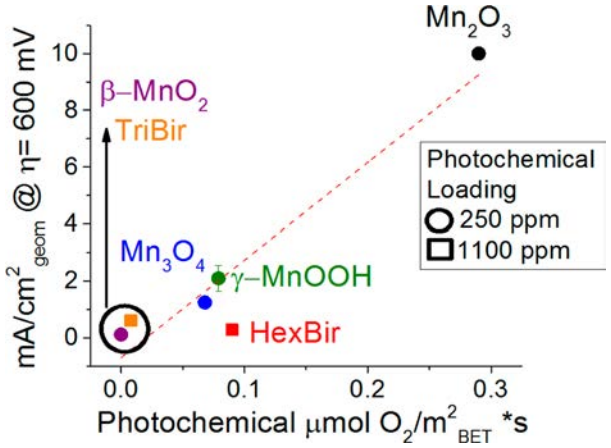

Figure 8. Current densities obtained from voltammetry (normalized to geometric electrode area) of Mn oxide compounds (fixed loading of 0.5 mg/cm^2 electrode area) plotted versus the photochemical O_2 evolution rate measured in solution (normalized to catalyst surface area obtained by BET). Data are the average of three replicates. Error bars are depicted but for most cases are contained in the symbol size. All data are for pH 7. Electrochemical conditions are described in Figure 3. Photochemical results for Mn_2O_3, Mn_3O_4, and β-MnO_2 are taken from ref 4.

Edge- vs Corner-Sharing Octahedra in Birnessites. As a third investigation of edge- vs corner-shared Mn^{3+}, we compared electrocatalysis using crystalline HexBir and TriBir samples. These samples had been previously synthesized, extensively characterized, and photochemically studied by our group in earlier reports[4,28] but have not been studied by electrocatalysis until now. Further, these samples are reported to have average Mn oxidation states 3.92 (HexBir)[58] and 3.63 (TriBir).[59]

In comparison to γ-MnOOH under photochemical assay conditions at 250 ppm loading, neither birnessite produces O_2 above our detection limit (Figure 7, left), consistent with our previous reports.[4,28] Electrochemically, both birnessites are poor electrocatalysts, on par with β-MnO_2. Neither birnessite produced 1 mA/cm^2 current density below an applied potential of 600 mV, at neither alkaline nor neutral pH (Figure 8 and Figure S15 in the Supporting Information). To our knowledge, no layered Mn oxide can achieve 10 mA/cm^2 below 600 mV overpotential, confirming again that neither edge- nor face-shared MnO_6 octahedra are active catalytic sites.

A difference in activity between these birnessites can be seen using the photochemical assay only at very high loading to enable detection of O_2 above the limit of detection. At ∼4.5-fold higher loading (1100 ppm), and following an ∼60 s lagtime for both materials, HexBir produced noticeably more O_2 than TriBir (initial rates 0.09 vs 0.008 μmol O_2/m^2_{BET}, Figure 7, right). Our results thus show that activity does not necessarily correlate with total Mn^{3+} content but, more likely, with the content of corner-shared Mn^{3+} sites. In particular, birnessites with Mn^{3+} located in the interlayer/surface (hexagonal type) are more active than Mn^{3+} located in edge-

DOI: 10.1021/acscatal.6b00099
ACS Catal. 2016, 6, 2089−2099

sharing sheets (triclinic type). The light-driven assay method appears to be valuable to demonstrate activity from crystalline birnessite, as other layered materials are known to be active only under illumination.[60,61] While the mechanism of photoactivation of birnessite is not well understood, recent data suggest that more corner-sharing Mn^{3+} are formed in the process.[62]

DISCUSSION

Earlier[4,28] and present results show a positive correlation between water oxidation activity and surface-directed, corner-sharing Mn^{3+}. In contrast, no catalytic activity is found for layered edge-sharing Mn^{3+} or Mn^{4+} oxides in any coordination environment. For example, sparse Mn^{3+} sites, but not bulk Mn^{4+} sites, are the oxidizing centers in birnessites for catalytic oxidation of phenols, sulfides, and metals (e.g., Cr^{3+}).[63,64] Analogously, phenol oxidation occurs readily on γ-MnOOH but not on β-MnO_2.[65] The reverse, the oxygen reduction reaction, is also highly dependent on octahedral Mn^{3+} sites.[66] Conclusions that one can take away from these works are as follows: surface Mn^{3+}−O bonds are kinetically labile to ligand substitution, thus enabling ligand exchange to inner-sphere sites where oxidation can occur. This lability is attributed to the presence of an electron in an antibonding 3d* orbital (discussed below). In contrast, Mn^{4+}−O bonds lack this electron and are exchange inert, preventing inner-sphere complex formation. Accordingly, inner-sphere substrate exchange is too slow for Mn^{4+} and blocks catalytic turnover.

The binding of water molecules to birnessites provides further insight. Studies of $K_{0.231}Mn^{3+}_{0.077}(Mn^{4+}_{0.885}\square_{0.115})O_2 \cdot 0.6\ H_2O$ ($\square$ represents lattice vacancies) by Lanson et al. assigned 40% of the formula water molecules as bound to interlayer (corner-shared) Mn^{3+}, despite being present as only 9% of the total Mn.[58] Accordingly, we envision that layered birnessites are poor at binding water unless corner-sharing Mn^{3+} are present on the surface. This proposed "active water surface" is generated simply by the equilibrium given in eq 1, in which Mn_{aq}^{2+} and MnO_2 interconvert with γ-MnOOH, topologically as shown in Scheme 1. The rearrangement can be viewed as displacement of an edge shared Mn^{4+} from within the layer to above the layer upon reduction by Mn^{2+}. This forms a surface $Mn^{3+}O_6$ that bridges to three corner oxos on a 3-fold axis of the octahedron and sits above an octahedral vacancy. As the comproportionation reaction continues to completion, this vacancy grows to become a rhombohedral tunnel (γ-MnOOH). Formation of γ-MnOOH is known to occur more rapidly on disordered, poorly crystalline layered materials than on rigid, crystalline materials,[20] suggesting a lower free energy path for the disordered (random) vs ordered sequence of displacement steps.

In a previous report we showed that bixbyite Mn_2O_3 has the highest activity of eight Mn oxides when it is tested in a photochemical assay and normalized to surface area.[4] Herein, we have extended that study by including γ-MnOOH, another 100% Mn^{3+} oxide, as well as by testing via electrochemical assay. We find that Mn_2O_3 is also the most active electrocatalyst but caution that electrochemically active surface area normalization is not well-defined in this assay.[67] In this study, Mn_2O_3 has a 1 order of magnitude higher capacitance than γ-MnOOH (Figure S16 in the Supporting Information), indicating that considerably more Mn_2O_3 is electrically accessible to non-Faradaic charging/polarization throughout the bulk. However, these measurements may not give a true estimate of amount of

Scheme 1. Depiction of Corner-Shared Mn^{3+} Octahedra in Birnessites (Top) and the S_2 Intermediate of Photosynthesis in Spin State 5/2 Tautomer (Bottom)

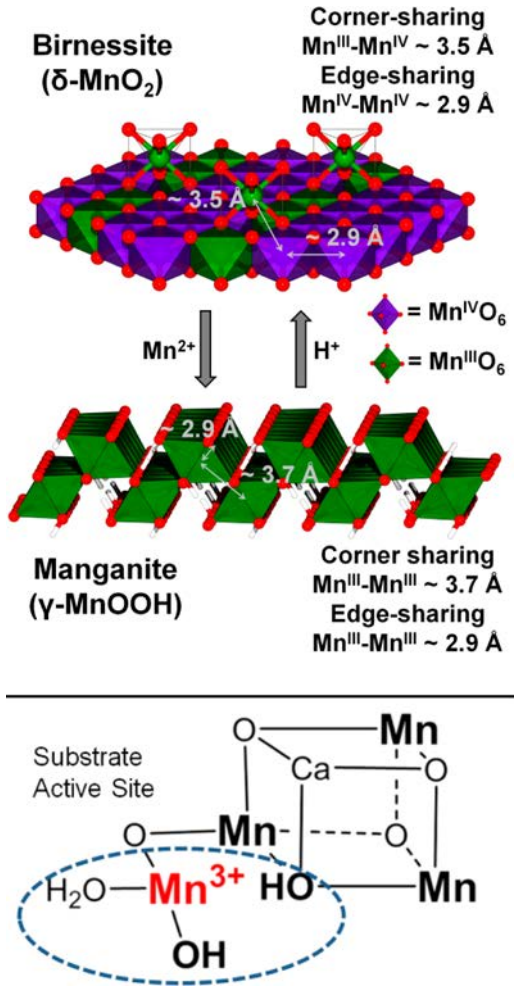

catalytic sites, which are surface specific.[67] Our results here show that Mn_2O_3 is more robust than γ-MnOOH to electrochemical cycling and also has an ~4-fold higher photochemical O_2 evolution rate when it is normalized to BET surface area. We thus consider Mn_2O_3 as having an intrinsically more active structure.

γ-MnOOH contains only one structural type of Mn^{3+} in the unit cell (Figure 9). This type of $Mn^{3+}O_6$ consists of tetragonally elongated (D_{4h}-type) octahedra as result of vibronic (Jahn−Teller) distortion, which is widely known to produce the lowest total energy (electronic + vibrational) for the d^4 electronic configuration. This distortion results in four short and two long Mn−OX bonds per D_{4h}-type octahedron (Mn−O at 1.88, 1.97, 2.21 Å and Mn−O(H) at 1.89, 1.98, 2.33 Å). Individual D_{4h} units are connected by corner-sharing bridges to three other $Mn^{3+}O_6$ and lie above a rhombohedral vacancy. The Mn−Mn distances (solid lines, Figure 9) are in the range 3.66−3.82 Å.

In contrast, Mn_2O_3 has a close-packed structure with shorter Mn−Mn distances (3.54−3.58 Å) and correspondingly higher gravimetric density (4.95 vs 4.3 g/mL for γ-MnOOH). It has five symmetry-inequivalent $Mn^{3+}O_6$ sites in the unit cell. In three of the five types, all Mn−O bond lengths are different (e.g., 1.88, 1.91, 1.97, 2.00, 2.22, 2.27 Å). These exhibit a large range (maximum difference 0.39 Å) with two short, two

DOI: 10.1021/acscatal.6b00099
ACS Catal. 2016, 6, 2089−2099

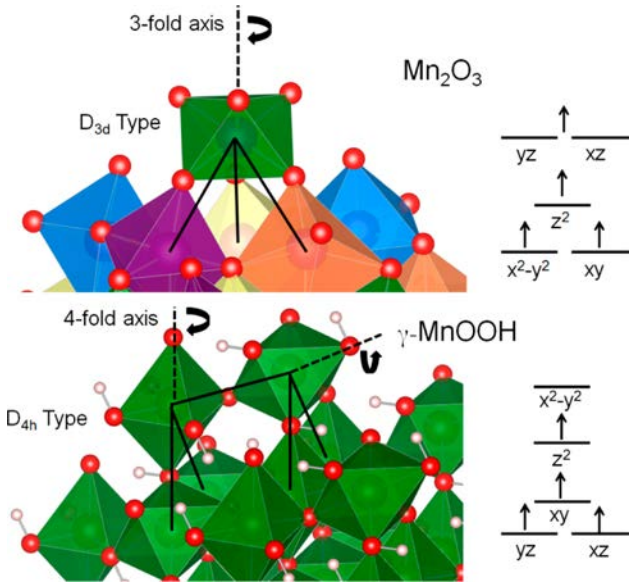

Figure 9. (left) Depiction of crystal structures of Mn_2O_3 and γ-MnOOH. These have structurally distinct types of surface $Mn^{3+}O_6$ "octahedra" that give rise to three nonbridging surface oxos (aquos/hydroxos) which represent potential substrate water binding sites during the catalytic cycle. In both cases the Mn center connects by corner-sharing bridges to three other Mn. However, these water binding sites differ in their binding affinity to Mn^{3+} and kinetic lability. Symmetry-inequivalent octahedra within the unit cell are denoted with different colors. See text. (right) Crystal field energies for the two types of surface $Mn^{3+}O_6$ units. See text for details.

intermediate, and two long bonds. This symmetry type is orthorhombic but is essentially treated here as distortion of the conventional tetragonal class (D_{4h}) with two long (trans) and four shorter (cis) bonds. In the remaining two types, all bond lengths are very similar and have an intermediate distance (e.g., 1.96, 1.99, 2.05 Å). This symmetry type is trigonal antiprismatic (D_{3d}). These sites additionally compare to the predominant γ-MnOOH motif in that they connect by corner-sharing bridges to two or three other $Mn^{3+}O_6$ (the latter is depicted in Figure 9). We highlight these sites as having special properties important for catalysis, as discussed next.

As shown in Figure 9 for Mn_2O_3, the surface $Mn^{3+}O_6$ sits above a 3-fold axis and so retains the D_{3d} symmetry enforced by the three oxo bridges (the ligand field). This creates an e_g* highest occupied molecular orbital (HOMO) that is doubly degenerate, antibonding, and comprised of d_{z^2} and $d_{x^2-y^2}$ orbitals on Mn and one sp^3 hybrid orbital on O. Hence, the ground electronic state has two equivalent antibonding orbital configurations (^{5}E state). The trigonal ligand field of the fixed oxo bridges suppresses the tetragonal Jahn–Teller distortion, and consequently the Mn–O bond lengths are expected to be nearly equivalent and intermediate in length, in agreement with the crystal structure. The three surface oxo sites where water can bind are expected to be relatively labile (more so than for the short cis bonds in the D_{4h} case), due to the antibonding electron. This could be a key contributor to the catalytic rate if release of O_2 from this site is rate-limiting: i.e., Mn^Vperoxo → Mn^{III} + O_2. This degenerate electronic configuration creates orbital angular momentum along the trigonal axis and therefore a coaxial force. This force introduces interesting possibilities for the mechanism of O–O bond formation and O_2 release which are beyond the scope of the present discussion.

The corresponding properties of the one type of $Mn^{3+}O_6$ unit in γ-MnOOH are quite different. Here there is a tetragonal elongation (along a 4-fold axis) resulting from the interaction of the d^4 electron configuration with the six oxygen ligands. These are made inequivalent by the electron vacancy in the half-filled shell occupying the $d_{x^2-y^2}$ orbital. This distortion produces two long and four short Mn–O bonds and removes the degeneracy of the e_g* orbital doublet. The electronic state splits into a lower (ground) state $^5B_{1g}$ (hole in $d_{x^2-y^2}$) and first excited state $^5A_{1g}$ (hole in d_{z^2}).

The vertical energy splitting, obtained from absorption spectra, is a measure of this distortion ($E(^5A_{1g}$-$^5B_{1g}) = 2E_{JT}$ = 1.77–1.38 eV for aquo and EDTA ligands, respectively).[68] This is the photon energy required to drive the pseudorotation of the *x,y,z* axes (interconversion of distortion axes). The corresponding thermal energy barrier for adiabatic pseudorotation on the ground state potential energy surface is called the Jahn–Teller trapping energy, E_{JT}. This value for trivalent Mn(III) fluoride complexes (e.g., $Mn(F)_2(\mu\text{-}F)_4$) is E_{JT} = 0.4–0.45 eV and is likely higher for stronger field hydroxo ligands.[69,70] Such a high energy barrier means that the tetragonal, D_{4h}-type distortion is deeply trapped and thermally activated pseudorotation is a very slow process at ambient temperatures. The water exchange rate at the two types of sites on surface $Mn^{3+}O_6$ differs greatly, with fast exchange for the one axial water site and very slow exchange for the two equatorial sites. This D_{4h} system has no orbital angular momentum in the ground state.

Finally, we note that the forgoing concepts are applicable to the catalytic site for photosynthetic water oxidation in photosystem II. Although two possible Mn oxidation state assignments have been proposed, supporters of *both* assignments have offered the S_2 state as containing a dangling Mn^{3+} with three water/hydroxo molecules within its inner coordination sphere (Scheme 1, bottom).[71,72] This dangling Mn^{3+} exists as a corner-shared species in the "closed cubane", spin = 5/2 tautomer which contains the only Mn-bound waters in the entire catalyst. By analogy to the results reported herein, we predict that the ligand environment around the dangling Mn is designed to disfavor formation of Mn^{4+}: i.e., favor Mn^{3+} and Mn^{5+} at this site in the full catalytic cycle. Thus, the same structural motif found in the two most active manganese oxide catalysts, Mn_2O_3 and γ-MnOOH, is present in the photosynthetic water oxidation site. We emphasize this structural commonality as a critical requirement for natural photosynthetic water oxidation. Further, nature's use of only four terminal water ligands (on Ca or Mn^{3+}, Scheme 1 bottom) in conjunction with eight amino acid ligands (on other Mn) highlights an effective strategy to prevent catalyst hydrolysis into stable Mn^{4+} oxides lacking catalytic activity. A successful water oxidation catalyst made from manganese must therefore prevent Mn^{3+} from oxidizing to Mn^{4+} at the substrate water binding site, a seemingly paradoxical finding considering the need to accumulate four holes for O_2 evolution. A simple way to prevent Mn^{3+} oxidation to Mn^{4+} is to destabilize it by preventing formation of the tetragonal MnO_6 geometry. This structural feature is indeed found in the dangling Mn site.[71,73] By shifting the potential energy of the valence d* antibonding orbitals to higher energy, the oxidation becomes more centered on oxide ligands (instead of Mn^{4+}). This description of the catalytic site frees the interpreter from using conventional tetragonal Mn^{3+} reference compounds as the main source for interpreting the complex spectroscopy of the OEC. We endorse

DOI: 10.1021/acscatal.6b00099
ACS Catal. 2016, 6, 2089–2099

future studies aimed at examining the properties of D_{3d} $Mn^{3+}O_6$ sites more fully.

In conclusion, a comparison of crystallographically distinct monophasic manganese oxides (herein and refs 4 and 28) shows a consistent trend indicating an advantage for Mn^{3+} in corner-sharing sites as catalytic centers for water oxidation, as opposed to edge-sharing Mn^{3+} and Mn^{4+} in either coordination. This structural requirement reconciles the description of Mn^{3+} content,[11] layer vacancies,[24] and 3.45 Å Mn−Mn distances[23] previously proposed as activity descriptors in other Mn oxides.

EXPERIMENTAL SECTION

Materials. All solutions were prepared with reagent grade water (18 MΩ, Hydro Picopure). All solvents and reagents were reagent grade, purchased commercially and used without further purification. This study utilized bixbyite (Mn_2O_3, 16.3 m^2/g), pyrolusite (β-MnO_2, 14.9 m^2/g), and hausmannite (Mn_3O_4, 27.2 m^2/g), which have been described previously.[4] Tested birnessites for this study included triclinic δ-MnO_2 (17.9 m^2/g)[4] and HexBir (5 m^2/g);[28] 20% Ir@C (vulcanized) was purchased from Premetek.

Preparation of Manganite (γ-MnOOH). A literature procedure[31] was adapted as follows. A 1 M HNO_3 solution (40 mL) containing 2 g of sucrose was stirred at room temperature, and 200 mL of water containing 5.89 g of $KMnO_4$ was added, followed by 4.4 g of $MnSO_4 \cdot H_2O$. The solution was refluxed for 6 h. Hot filtration recovered a brown solid, which was washed with water and air-dried. Note: γ-MnOOH is not stable above 250 °C.

Electrochemistry. A CH Instruments Electrochemical Workstation was used. Neutralized Nafion (working) electrodes were prepared using a modification of the procedure of Shao-Horn et al.:[74] A solution of Nafion (5%) was brought to pH 7 by addition of ∼1/2 volume equiv of 0.1 M NaOH. This Nafion was diluted with ethanol and water in a volume ratio of 4:4:5. To this solution were added acetylene black (1 mg/mL) and Mn oxide (20 mg/mL), and the mixture was dispersed via sonication. For most measurements, 5 μL of the suspension was dropcast on a 5 mm diameter glassy-carbon electrode.

The resulting electrochemical current from these catalyst-film electrodes was normalized to the geometric area, the BET determined gas adsorption surface area, or the electrochemical charge surface area from capacitance. For large-scale measurements of Faradaic efficiency, and to isolate the postreaction product, 200 μL was dropcast onto 1.5 × 1.5 cm stainless steel mesh (pretreated in 30% HNO_3 for 30 min), connected via Cu tape to Ti wire. Following analysis, films were sonicated into ethanol; water was added, and then the sample was centrifuged. Upon assembly, all electrodes had less than 10 Ω resistance at pH 14 and 20 Ω resistance at pH 7. CV's were *iR*-corrected (95%), initiated at the open circuit potential, and performed at 10 mV/s scan rate with vigorous stirring. Ti wire was used as a counter electrode. Reference electrodes were Ag/AgCl (pH 7) and Hg/HgO (pH 14). Silver reference electrodes were externally calibrated against the SCE, and the values did not deviate by more than 5 mV. Overpotentials were calculated by overpotential = (measured potential) − (1.23 V − (0.059 × pH) − E(reference electrode)) using +0.100 V for Hg/HgO and +0.240 V for SCE. Tafel slopes were recorded on a PINE rotating-disk electrode setup.

Powder X-ray Diffraction (PXRD). Patterns were recorded on a Rigaku Ultima IV X-ray diffractometer, using Cu Kα radiation (λ = 1.5406 Å). A graphite monochromator was used, and the generator power settings were set to 40 kV and 44 mA. Data were collected at 2θ values of 3−50° with a step size of 0.02° and a scan speed of 2.5°/min.

BET. Surface area measurements were made by N_2 gas adsorption at 77 K on a volumetric gas sorption analyzer (Autosorb-1 MP, Quantachrome Instruments). A 100 mg portion of the sample was prepared by outgassing under vacuum at 120 °C for 1 h.

X-ray Photoelectron Spectroscopy (XPS). A Thermo K-Alpha spectrometer was used with charge compensation; spectra were calibrated against adventitious carbon. Solid samples were fixed on carbon tape, and a beam of 150 μm diameter was focused on an area covered by the powdered sample. In order to deconvolute the Mn $2p_{3/2}$ spectra, we followed the precedent set by Nesbitt and Banerjee.[55] Each oxidation state of Mn results in a set of 5 multiplets (15 total); relative peak intensities and differences in binding energies (ΔeV) from peak to peak were set as fixed values (the highest energy multiplet of Mn^{4+} was allowed variable intensity) on the basis of the values used in their study and those calculated by Gupta and Sen. The lowest energy Mn^{4+} multiplet was used as a reference point to set the binding energy of the lowest energy Mn^{3+} and Mn^{2+} multiplets at fixed values. The other four higher energy multiplets of each group were set at a specific ΔeV value from the lowest energy peaks but were allowed a 0.2 eV variance. These same ΔeV values were used for each sample measured. The full widths at half-maximum (fwhm) were constrained to a specific value for each sample (30% Lorentzian/70% Gaussian), ranging from 1.16 to 1.23 eV. The initial peak position for Mn^{4+} was determined from our reference sample, β-MnO_2, and the O 1s spectra peak maxima were used to calibrate the Mn^{4+} position for the other samples.

Scanning and Transmission Electron Microscopy (SEM, TEM). A JEOL 2010F TEM/STEM instrument with EDS and EELS attachments was used for the high-resolution (HRTEM) and electron diffraction (SAED) microscopy observations. The scope was operated at 200 keV with a resolution better than 1.5 Å in both imaging and scanning modes. SEM measurements were performed on a FEI Quanta 200 FEG Environmental-Scanning Electron Microscope. ICP analysis was performed on a PerkinElmer Optima 7300 ICP-OES instrument.

Raman Spectroscopy. Raman spectra were collected with a Renishaw InVia Raman microscope using a 514 nm laser excitation line with power varying between 1.5 and 15 mW, with accumulation of the signal for 10, 60, or 300 s. The spectra were collected between 100 and 2000 cm^{-1} using a grating with 1800 lines/mm. The sample was focused using a 50× short working distance objective with NA 0.75. Each measurement was collected in triplicate for statistical significance. Confocal measurements were collected in high confocality modality with depths varying between 0.1 and 10 μm.

O_2 Evolution. A Clark-type oxygen electrode (Hansatek Ltd.) was used to obtain oxygen rates and yields. It was calibrated daily using N_2-deoxygenated and air-saturated solutions. Manganese oxide powders were dispersed in bicarbonate buffered aqueous solution (0.1 M pH 7) containing $Ru(bpy)_3^{2+}$ (0.5 mM) and $Na_2S_2O_8$ (10 mM) and subjected to visual light illumination (the light profile is described in ref 75).

DOI: 10.1021/acscatal.6b00099
ACS Catal. 2016, 6, 2089−2099

■ ASSOCIATED CONTENT

Supporting Information

The Supporting Information is available free of charge on the ACS Publications website at DOI: 10.1021/acscatal.6b00099.

Supplemental characterization of before and after samples, as well as electrochemical activity measurements and surface Mn population (PDF)

■ AUTHOR INFORMATION

Corresponding Author

*E-mail for G.C.D.: dismukes@rutgers.edu.

Notes

The authors declare no competing financial interest.

■ ACKNOWLEDGMENTS

This work was supported by NSF CLP #1213772. We are grateful to NSF DGE0903675 for IGERT fellowships (P.F.S, G.G.). B.J.D., H.W., and J.L. acknowledge partial support by the U.S. Department of Energy, Office of Basic Energy Sciences, Materials Sciences and Engineering Division, through grant DE-FG02-08ER46491 for materials characterization, including PXRD, XPS, and BET surface area analysis. We thank Dr. Anders B. Laursen for valuable discussions and SEM images and Karin Calvinho for ICP measurements.

■ REFERENCES

(1) Yamaguchi, A.; Inuzuka, R.; Takashima, T.; Hayashi, T.; Hashimoto, K.; Nakamura, R. *Nat. Commun.* **2014**, *5*, 4256.

(2) Park, J.; Kim, H.; Jin, K.; Lee, B. J.; Park, Y.-S.; Kim, H.; Park, I.; Yang, K. D.; Jeong, H.-Y.; Kim, J.; Hong, K. T.; Jang, H. W.; Kang, K.; Nam, K. T. *J. Am. Chem. Soc.* **2014**, *136*, 4201−4211.

(3) Kuo, C.-H.; Mosa, I. M.; Poyraz, A. S.; Biswas, S.; El-Sawy, A. M.; Song, W.; Luo, Z.; Chen, S.-Y.; Rusling, J. F.; He, J.; Suib, S. L. *ACS Catal.* **2015**, *5*, 1693−1699.

(4) Robinson, D. M.; Go, Y. B.; Mui, M.; Gardner, G.; Zhang, Z.; Mastrogiovanni, D.; Garfunkel, E.; Li, J.; Greenblatt, M.; Dismukes, G. C. *J. Am. Chem. Soc.* **2013**, *135*, 3494−3501.

(5) Gorlin, Y.; Jaramillo, T. F. *J. Am. Chem. Soc.* **2010**, *132*, 13612−13614.

(6) Cady, C. W.; Gardner, G.; Maron, Z. O.; Retuerto, M.; Go, Y. B.; Segan, S.; Greenblatt, M.; Dismukes, G. C. *ACS Catal.* **2015**, *5*, 3403−3410.

(7) Morita, M.; Iwakura, C.; Tamura, H. *Electrochim. Acta* **1979**, *24*, 357−362.

(8) Mattioli, G.; Zaharieva, I.; Dau, H.; Guidoni, L. *J. Am. Chem. Soc.* **2015**, *137*, 10254−10267.

(9) McKendry, I. G.; Kondaveeti, S. K.; Shumlas, S. L.; Strongin, D. R.; Zdilla, M. J. *Dalt. Trans.* **2015**, *44*, 12981−12984.

(10) Jeong, D.; Jin, K.; Jerng, S. E.; Seo, H.; Kim, D.; Nahm, S. H.; Kim, S. H.; Nam, K. T. *ACS Catal.* **2015**, *5*, 4624−4628.

(11) Takashima, T.; Hashimoto, K.; Nakamura, R. *J. Am. Chem. Soc.* **2012**, *134*, 1519−1527.

(12) Indra, A.; Menezes, P. W.; Driess, M. *ChemSusChem* **2015**, *8*, 776−785.

(13) Dismukes, G. C.; Brimblecombe, R.; Felton, G. A. N.; Pryadun, R. S.; Sheats, J. E.; Spiccia, L.; Swiegers, G. F. *Acc. Chem. Res.* **2009**, *42*, 1935−1943.

(14) Ruettinger, W.; Yagi, M.; Wolf, K.; Bernasek, S.; Dismukes, G. C. *J. Am. Chem. Soc.* **2000**, *122*, 10353−10357.

(15) Luo, J.; Zhang, Q.; Suib, S. L. *Inorg. Chem.* **2000**, *39*, 741−747.

(16) Elzinga, E. J. *Environ. Sci. Technol.* **2011**, *45*, 6366−6372.

(17) Portehault, D.; Cassaignon, S.; Baudrin, E.; Jolivet, J.-P. *Cryst. Growth Des.* **2010**, *10*, 2168−2173.

(18) Luo, J.; Huang, A.; Park, S. H.; Suib, S. L.; O'Young, C.-L. *Chem. Mater.* **1998**, *10*, 1561−1568.

(19) Lefkowitz, J. P.; Rouff, A. A.; Elzinga, E. J. *Environ. Sci. Technol.* **2013**, *47*, 10364−10371.

(20) Elzinga, E. J.; Kustka, A. B. *Environ. Sci. Technol.* **2015**, *49*, 4310−4316.

(21) Robinson, D. M.; Go, Y. B.; Greenblatt, M.; Dismukes, G. C. *J. Am. Chem. Soc.* **2010**, *132*, 11467−11469.

(22) Kohler, T.; Armbruster, T.; Libowitzky, E. *J. Solid State Chem.* **1997**, *133*, 486−500.

(23) Zaharieva, I.; Chernev, P.; Risch, M.; Klingan, K.; Kohlhoff, M.; Fischer, A.; Dau, H. *Energy Environ. Sci.* **2012**, *5*, 7081−7089.

(24) Iyer, A.; Del-Pilar, J.; King'ondu, C. K.; Kissel, E.; Garces, H. F.; Huang, H.; El-Sawy, A. M.; Dutta, P. K.; Suib, S. L. *J. Phys. Chem. C* **2012**, *116*, 6474−6483.

(25) Wiechen, M.; Zaharieva, I.; Dau, H.; Kurz, P. *Chem. Sci.* **2012**, *3*, 2330−2339.

(26) Zaharieva, I.; Najafpour, M. M.; Wiechen, M.; Haumann, M.; Kurz, P.; Dau, H. *Energy Environ. Sci.* **2011**, *4*, 2400−2408.

(27) Menezes, P. W.; Indra, A.; Littlewood, P.; Schwarze, M.; Göbel, C.; Schomäcker, R.; Driess, M. *ChemSusChem* **2014**, *7*, 2202−2211.

(28) Deibert, B. J.; Zhang, J.; Smith, P. F.; Chapman, K. W.; Rangan, S.; Banerjee, D.; Tan, K.; Wang, H.; Pasquale, N.; Chen, F.; Lee, K.-B.; Dismukes, G. C.; Chabal, Y. J.; Li, J. *Chem. - Eur. J.* **2015**, *21*, 14218−14228.

(29) Pokhrel, R.; Goetz, M. K.; Shaner, S. E.; Wu, X.; Stahl, S. S. *J. Am. Chem. Soc.* **2015**, *137*, 8384−8387.

(30) El-Deab, M. S.; Awad, M. I.; Mohammad, A. M.; Ohsaka, T. *Electrochem. Commun.* **2007**, *9*, 2082−2087.

(31) Crisostomo, V. M. B.; Ngala, J. K.; Alia, S.; Dobley, A.; Morein, C.; Chen, C.-H.; Shen, X.; Suib, S. L. *Chem. Mater.* **2007**, *19*, 1832−1839.

(32) Gao, T.; Krumeich, F.; Nesper, R.; Fjellvåg, H.; Norby, P. *Inorg. Chem.* **2009**, *48*, 6242−6250.

(33) Bernard, M.; Hugot-Le Goff, A.; Thi, B. V.; Cordoba de Torresi, S. *J. Electrochem. Soc.* **1993**, *140*, 3065−3070.

(34) Morris, N. D.; Suzuki, M.; Mallouk, T. E. *J. Phys. Chem. A* **2004**, *108*, 9115−9119.

(35) Ramstedt, M.; Sjöberg, S. *Aquat. Geochem.* **2005**, *11*, 413−431.

(36) Ramstedt, M.; Shchukarev, A. V.; Sjöberg, S. *Surf. Interface Anal.* **2002**, *34*, 632−636.

(37) Ramstedt, M.; Andersson, B. M.; Shchukarev, A.; Sjöberg, S. *Langmuir* **2004**, *20*, 8224−8229.

(38) Bricker, O. *Am. Mineral.* **1965**, *50*, 1296−1354.

(39) McCrory, C. C. L.; Jung, S.; Peters, J. C.; Jaramillo, T. F. *J. Am. Chem. Soc.* **2013**, *135*, 16977−16987.

(40) McCrory, C. C. L.; Jung, S.; Ferrer, I. M.; Chatman, S. M.; Peters, J. C.; Jaramillo, T. F. *J. Am. Chem. Soc.* **2015**, *137*, 4347−4357.

(41) Boppana, V. B. R.; Jiao, F. *Chem. Commun.* **2011**, *47*, 8973−8975.

(42) Meng, Y.; Song, W.; Huang, H.; Ren, Z.; Chen, S.-Y.; Suib, S. L. *J. Am. Chem. Soc.* **2014**, *136*, 11452−11464.

(43) Fekete, M.; Hocking, R. K.; Chang, S. L. Y.; Italiano, C.; Patti, A. F.; Arena, F.; Spiccia, L. *Energy Environ. Sci.* **2013**, *6*, 2222−2232.

(44) Cua, A.; Vrettos, J. S.; de Paula, J. C.; Brudvig, G. W.; Bocian, D. F. *J. Biol. Inorg. Chem.* **2003**, *8*, 439−451.

(45) Sheats, J. E.; Czernuszewicz, R. S.; Dismukes, G. C.; Rheingold, A. L.; Petrouleas, V.; Stubbe, J.; Armstrong, W. H.; Beer, R. H.; Lippard, S. J. *J. Am. Chem. Soc.* **1987**, *109*, 1435−1444.

(46) Julien, C.; Massot, M.; Poinsignon, C. *Spectrochim. Acta, Part A* **2004**, *60*, 689−700.

(47) Ammundsen, B.; Burns, G. R.; Islam, M. S.; Kanoh, H.; Rozière, J. *J. Phys. Chem. B* **1999**, *103*, 5175−5180.

(48) Postorino, P.; Congeduti, A.; Degiorgi, E.; Itié, J. P.; Munsch, P. *Phys. Rev. B: Condens. Matter Mater. Phys.* **2002**, *65*, 224102.

(49) Dave, B. C.; Czernuszewicz, R. S. *Inorg. Chim. Acta* **1998**, *281*, 25−35.

(50) Amalraj, S. F.; Sharon, D.; Talianker, M.; Julien, C. M.; Burlaka, L.; Lavi, R.; Zhecheva, E.; Markovsky, B.; Zinigrad, E.; Kovacheva, D.; Stoyanova, R.; Aurbach, D. *Electrochim. Acta* **2013**, *97*, 259−270.

(51) Dong, Y.; Li, K.; Jiang, P.; Wang, G.; Miao, H.; Zhang, J.; Zhang, C. *RSC Adv.* **2014**, *4*, 39167−39173.
(52) Gao, T.; Fjellvåg, H.; Norby, P. *Anal. Chim. Acta* **2009**, *648*, 235−239.
(53) Xing, X. J.; Yu, Y. P.; Xu, L. M.; Wu, S. X.; Li, S. W. *J. Phys. Chem. C* **2008**, *112*, 15526−15531.
(54) Bulavchenko, O. A.; Vinokurov, Z. S.; Afonasenko, T. N.; Tsyrul'nikov, P. G.; Tsybulya, S. V.; Saraev, A. A.; Kaichev, V. V. *Dalt. Trans.* **2015**, *44*, 15499−15507.
(55) Nesbitt, H. W. W.; Banerjee, D. *Am. Mineral.* **1998**, *83*, 305−315.
(56) Toupin, M.; Brousse, T.; Bélanger, D. *Chem. Mater.* **2004**, *16*, 3184−3190.
(57) Ramírez, A.; Hillebrand, P.; Stellmach, D.; May, M. M.; Bogdanoff, P.; Fiechter, S. *J. Phys. Chem. C* **2014**, *118*, 14073−14081.
(58) Gaillot, A.-C.; Flot, D.; Drits, V. a.; Manceau, A.; Burghammer, M.; Lanson, B. *Chem. Mater.* **2003**, *15*, 4666−4678.
(59) Ching, S.; Landrigan, J. A.; Jorgensen, M. L. *Chem. Mater.* **1995**, *7*, 1604−1606.
(60) Singh, A.; Hocking, R. K.; Chang, S. L.-Y.; George, B. M.; Fehr, M.; Lips, K.; Schnegg, A.; Spiccia, L. *Chem. Mater.* **2013**, *25*, 1098−1108.
(61) Hocking, R. K.; Brimblecombe, R.; Chang, L.-Y.; Singh, A.; Cheah, M. H.; Glover, C.; Casey, W. H.; Spiccia, L. *Nat. Chem.* **2011**, *3*, 461−466.
(62) Marafatto, F. F.; Strader, M. L.; Gonzalez-Holguera, J.; Schwartzberg, A.; Gilbert, B.; Peña, J. *Proc. Natl. Acad. Sci. U. S. A.* **2015**, *112*, 4600−4605.
(63) Nico, P. S.; Zasoski, R. J. *Environ. Sci. Technol.* **2001**, *35*, 3338−3343.
(64) Nico, P. S.; Zasoski, R. J. *Environ. Sci. Technol.* **2000**, *34*, 3363−3367.
(65) Ukrainczyk, L.; Mcbride, M. B. *Clays Clay Miner.* **1992**, *40*, 157−166.
(66) Stoerzinger, K. A.; Risch, M.; Han, B.; Shao-Horn, Y. *ACS Catal.* **2015**, *5*, 6021−6031.
(67) Jung, S.; McCrory, C. C. L.; Ferrer, I. M.; Peters, J. C.; Jaramillo, T. F. *J. Mater. Chem. A* **2016**, *4*, 3068.
(68) Davis, T. S.; Fackler, J. P.; Weeks, M. J. *Inorg. Chem.* **1968**, *7*, 1994−2002.
(69) Reinen, D.; Atanasov, M.; Massa, W. *Z. Anorg. Allg. Chem.* **2006**, *632*, 1375−1398.
(70) Reinen, D.; Atanasov, M.; Köhler, P.; Babel, D. *Coord. Chem. Rev.* **2010**, *254*, 2703−2754.
(71) Vinyard, D. J.; Ananyev, G. M.; Dismukes, G. C. *Annu. Rev. Biochem.* **2013**, *82*, 577−606.
(72) Krewald, V.; Retegan, M.; Cox, N.; Messinger, J.; Lubitz, W.; DeBeer, S.; Neese, F.; Pantazis, D. a. *Chem. Sci.* **2015**, *6*, 1676−1695.
(73) Petrie, S.; Pace, R. J.; Stranger, R. *Angew. Chem.* **2015**, *127*, 7226−7230.
(74) Suntivich, J.; Gasteiger, H. A.; Yabuuchi, N.; Shao-Horn, Y. *J. Electrochem. Soc.* **2010**, *157*, B1263−B1268.
(75) Smith, P. F.; Kaplan, C.; Sheats, J. E.; Robinson, D. M.; McCool, N. S.; Mezle, N.; Dismukes, G. C. *Inorg. Chem.* **2014**, *53*, 2113−2121.

DOI: 10.1021/acscatal.6b00099
ACS Catal. 2016, 6, 2089−2099